

Redshift Space Distortion of 21cm line at $1 < z < 5$ with Cosmological Hydrodynamic Simulations

Rika Ando¹, ^{*} Atsushi J. Nishizawa^{1,2}, [†] Kenji Hasegawa¹, Ikkoh Shimizu³ and Kentaro Nagamine^{3,4,5}

¹ Department of Physics, Nagoya University, Furocho, Chikusa, Nagoya, Aichi 464-8602, Japan,

² Institute for Advanced Research, Nagoya University, Furosho, Chikusa, Nagoya, Aichi 464-8602, Japan,

³ Department of Earth and Space Science, Graduate School of Science, Osaka University, 1-1 Machikaneyama, Toyonaka, Osaka 560-0043, Japan

⁴ Department of Physics and Astronomy, University of Nevada, Las Vegas, 4505 S.Maryland Pkwy, Las Vegas, NV, 89154-4002, USA

⁵ Kavli IPMU, The University of Tokyo, 5-1-5 Kashiwanoha, Kashiwa, Chiba, 277-8583, Japan

14 December 2024

ABSTRACT

We measure the scale dependence and redshift dependence of 21 cm line emitted from the neutral hydrogen gas at redshift $1 < z < 5$ using full cosmological hydrodynamic simulations by taking the ratios between the power spectra of H I–dark matter cross correlation and dark matter auto-correlation. The neutral hydrogen distribution is computed in full cosmological hydrodynamic simulations including star formation and supernova feedback under a uniform ultra-violet background radiation. We find a significant scale dependence of H I bias at $z > 3$ on scales of $k \gtrsim 1h\text{Mpc}^{-1}$, but it is roughly constant at lower redshift $z < 3$. The redshift evolution of H I bias is relatively slow compared to that of QSOs at similar redshift range. We also measure a redshift space distortion (RSD) of H I gas to explore the properties of H I clustering. Fitting to a widely applied theoretical prediction, we find that the constant bias is consistent with that measured directly from the real-space power spectra, and the velocity dispersion is marginally consistent with the linear perturbation prediction. Finally we compare the results obtained from our simulation and the Illustris simulation, and conclude that the detailed astrophysical effects do not affect the scale dependence of H I bias very much, which implies that the cosmological analysis using 21 cm line of H I will be robust against the uncertainties arising from small-scale astrophysical processes such as star formation and supernova feedback.

1 INTRODUCTION

The acceleration of the Universe has been one of the greatest mysteries since it was first discovered by the observations of type Ia supernovae (Perlmutter et al. 1999). One of the most natural explanations of the accelerated expansion is the dark energy in the regime of general relativity or modified theory of gravity (e.g. Clifton et al. 2012, for review). Because the acceleration only becomes effective at the late epoch of $z \lesssim 1$, the most promising probe of dark energy or modified gravity is the large-scale structure of the Universe.

Baryon acoustic oscillation (BAO) is recognized as a useful technique which is least affected by the systematics to constrain the dark energy models (e.g. Albrecht et al. 2006). After the first detection of BAO by the clustering of luminous red galaxies (LRG) in the Sloan Digital Sky Survey (SDSS) (Eisenstein et al. 2005), significant attention has been paid to constrain the dark energy through the power spectrum and the correlation function of BAO (e.g. Ross et al. 2015; Beutler et al. 2011). As the BAO is a measurement of the oscillation peak scales, an accurate prediction of the peak scales is required. It is well known that the oscillation peak scale is readily changed by the non-linear clustering of matter (Nishimichi et al. 2007) or the non-trivial couplings among different fluctuation modes due to galaxy bias (e.g. Cole et al. 2005; Dalal et al.

2008; McDonald & Roy 2009). Another important aspect of the BAO is the combination of parallel and perpendicular components to the line of sight (Alcock & Paczynski 1979). Although the AP-test makes the BAO a more powerful tool to constrain cosmological parameters, the systematic effect due to redshift space distortion (RSD) has to be taken into account as it is degenerate with the AP effect.

As we can observe galaxies only in redshift space, the distance to the galaxies are contaminated by the peculiar velocities of galaxies; on large scales, galaxies are coherently attracted toward the overdensity regions which makes the anisotropic two dimensional correlation function squashed, while on small scales, non-linear random motion makes correlation function elongated along the line of sight (e.g. Matsubara 2004). The RSD is important not only for correctly understanding the distortion of the correlation function to utilize the AP effects in the BAO, but also to gain an independent cosmological information from the BAO. Since the RSD is a direct measure of the velocity field, it is sensitive to the potential fluctuation Φ and thus to the theory of modified gravity (e.g. Hamilton 1998, for review).

The current measurements of the BAO and RSD have been mainly focused on the galaxy or QSO distribution as they are con-

sidered to be good tracers of the large-scale structure (Kirshner et al. 1981; Alam et al. 2017; Padmanabhan et al. 2007; de la Torre et al. 2017; Zhao et al. 2016; Busca et al. 2013; Slosar et al. 2011). However, due to the difficulty of taking the spectrum to accurately measure the redshift of the sources, we have studied the BAO only at $z < 3$. The first detection of the reionisation absorption signature by the EDGES observation of 21 cm line absorption associated with neutral hydrogen (HI) gas (Bowman et al. 2018) has also opened a new window to probe the large-scale structure. Even after the epoch of reionisation, some fraction of neutral hydrogen is confined within the high-density regions such as inside the galaxies preventing the ultra-violet photons to penetrate. Several surveys to map the 21 cm distribution by intensity mapping are proposed where individual objects are not resolved but a continuous smoothed sky distribution is mapped out. For example, the Square Kilometer Array (SKA) will cover the 25,000 (SKA1) square degree of sky with 50kHz frequency resolution, which is adequate for accurate redshifts at $0.35 < z < 3.06$ (for SKA1-MID), but with a moderately coarse angular resolution for the single-dish observation (Santos et al. 2015; Bull et al. 2015). There are interferometer mode in SKA which has significantly better angular resolution (depends on the configuration), however, its small field of view is not suited for a wide sky coverage and thus for cosmological analyses. Another example is the Baryon acoustic oscillations In Neutral Gas Hydrogen (BINGO) which will target much lower redshifts at $0.13 < z < 0.48$ (Battye et al. 2012). BINGO will cover 15×200 square degree of sky with 1MHz frequency resolution with a resolution of 40 arcmin for single-dish observation.

Much attention has been paid to the cosmological application of HI observations (e.g. Camera et al. 2015; Bull et al. 2015; Raccañelli et al. 2015; Olivari et al. 2018; Villaescusa-Navarro et al. 2017; Obuljen et al. 2018; Dinda et al. 2018). It has been shown that the Square Kilometer Array (SKA) has a capability to constrain the dark energy parameters comparable to that from the galaxy redshift surveys such as Euclid Bull et al. (2015) which is a Stage-IV survey according to the Dark Energy Task Force (Albrecht et al. 2006). However, it is also shown that the difficulty of the HI observation lies in the foreground removal (e.g. Wyithe et al. 2005) and in the modeling of HI bias. As in the case for galaxies or QSOs, it is important to understand the connection between HI gas and dark matter distribution, as theoretical predictions are often only for dark matter, the most dominant component of matter in terms of gravitational interaction. While Bull et al. (2015) assumed the simplest constant bias, Umeh (2017) found that the non-linear coupling between different fluctuation modes or shot-noise can modulate the amplitude of power spectrum even on large scales. Therefore, considering more realistic models or measurements from numerical simulations is of great importance for robust cosmological analyses. To predict the HI bias, halo model approach has been considered (Padmanabhan et al. 2017; Pénin et al. 2018), and several work have been done using pure N-body simulations (Sarkar et al. 2016; Sarkar & Bharadwaj 2018). They do not fully solve the radiative transfer but populate the HI according to the mass of the host dark matter halo.

In this paper, we measure the scale- and redshift-dependent HI bias using the full cosmological hydrodynamic simulation developed by the Osaka group, which takes gas dynamics into account with an appropriate UV background radiation and star formation with supernova feedback. We also perform the same analyses using the publicly released data of the Illustris simulation, and compare with our results to examine the impact of AGN feedback on the cosmological signals.

This paper is organized as follows. In Section 2, we describe the details of cosmological hydrodynamic simulations used in this work, and explain how we generate the mock HI data based on these simulations. In Section 3, we show the results for measuring the HI bias in real space to explore the redshift and scale dependence of the bias. In Section 4, we show the anisotropic HI power spectra in redshift space, and compared them with the linear and non-linear clustering modes. Section 5 is devoted to the interpretations of our results, and then we give a summary in Section 6. Throughout this paper, we assume the cosmological parameters consistent with the WMAP-9 year result (Hinshaw et al. 2013).

2 SIMULATION

In this section, we give a brief summary of two cosmological hydrodynamic simulations that we use in this paper, and describe how we make the mock simulated data targeting the future 21 cm observations.

2.1 Illustris simulation

One of the data set we use to evaluate the HI bias is from the cosmological hydrodynamic simulation Illustris,¹ in which the thermal and dynamical evolution of baryons is solved with a moving-mesh code AREPO (Springel 2010; Genel et al. 2014; Vogelsberger et al. 2014). We use the data set of Illustris simulation-3: the box-size is $75 h^{-1} \text{Mpc}$ on a side, 2×455^3 gaseous cells and dark matter (DM) particles are distributed in the volume. The Illustris simulation adopts the WMAP-9 cosmological parameters (Hinshaw et al. 2013): $\Omega_m = 0.2726$, $\Omega_\Lambda = 0.7274$, $\Omega_b = 0.0456$, $\sigma_8 = 0.809$, $n_s = 0.963$, $h = 0.704$. The resultant mass resolution is $5.70 \times 10^7 h^{-1} M_\odot$ for gas and $2.81 \times 10^8 h^{-1} M_\odot$ for DM (Nelson et al. 2015).

In the Illustris simulation, neutral hydrogen is ionized via photo-ionization and collisional ionization processes. The simulation employs a UV background (UVB) model of Faucher-Giguère et al. (2009) at $z < 6$. It is noted that the photo-ionization by the UVB mainly contributes to the heating on large scales. The gas temperature, which controls the collisional ionization rates, is determined by the competition between cooling and heating. The feedback driven by SNe and AGNs often heats the gas to above 10^5 K in the vicinities of galaxies, and consequently such regions are highly ionized via collisional ionization.

The SN feedback model in the Illustris simulation is basically the same as the wind model implemented in SPH-based schemes (e.g. Springel & Hernquist 2003; Oppenheimer & Davé 2008; Okamoto et al. 2010), except for a slight modification to account for mesh-based scheme (Vogelsberger et al. 2013; Torrey et al. 2014). As for the AGN feedback, the Illustris simulation adopts a two-state model, in which either radio-mode feedback or quasar-mode feedback is chosen according to the mass accretion rate onto a supermassive black hole (BH). When the BH accretion rate is high, quasar-mode feedback is activated so that a fraction (0.1–0.2) of the radiative energy released by the BH accretion is converted to the thermal energy. In the contrary case of low BH accretion rates, a jet launched from the BH mechanically affects the surrounding medium. In addition to these thermal and mechanical AGN feedback, the photo-heating and photo-ionization by the radiation from

¹ <http://www.illustris-project.org/>

AGNs are also considered (Vogelsberger et al. 2013; Torrey et al. 2014).

Although the feedback efficiencies are adjusted so as to reproduce the stellar mass function at the present-day and the cosmic star formation history (Genel et al. 2014), the AGN feedback in the Illustris simulation is known to be too strong, which resulted in the overheated IGM (Viel et al. 2017) and the hot gas was transported too far from galaxies (Haider et al. 2016).

2.2 Osaka simulation

The Osaka simulation uses a modified version of N-body/SPH code GADGET-3 (originally described by Springel 2005). Our code includes treatment for star formation and supernova feedback (but no AGN feedback), and the details can be found in Aoyama et al. (2017) and Shimizu et al. (2018, submitted). The uniform UV background radiation of Haardt & Madau (2012) is used, and the cooling is solved using the Grackle chemistry and cooling library (Smith et al. 2016).²

The simulation used in this paper has a box-size of comoving $85 h^{-1} \text{Mpc}$, and the initial particle number is 2×512^3 for gas and dark matter. The number of gas particles decreases slowly as some of them are converted into star particles in high-density regions. We use the same WMAP-9 cosmological parameters as the Illustris simulation for a fair comparison. The particle masses are $5.79 \times 10^7 h^{-1} M_{\odot}$ and $2.88 \times 10^8 h^{-1} M_{\odot}$ for gas and dark matter particles, which are roughly equivalent to those in the Illustris simulation.

Here we briefly review the prescription for star formation and SN feedback. The star formation is allowed when the local gas density exceeds the threshold density of $n_{\text{SF,th}} = 0.1 \text{ cm}^{-3}$, and two star particles can be created from each gas particle. The star particles are created statistically such that the time-averaged star formation rate (SFR) will recover the following rate:

$$\dot{\rho}_{\star} = \epsilon_{\star} \frac{\rho_{\text{gas}}}{t_{\text{ff}}}, \quad (1)$$

where we take $\epsilon_{\star} = 0.05$ and $t_{\text{ff}} = \sqrt{3\pi/(32G\rho_{\text{gas}})}$ is the local free-fall time. In this work, we do not consider the self-shielding correction, as we are not concerned too much about the small scales ($< 100 \text{ kpc}$) when we compute the power spectrum and the bias parameter. Once the star particle is created, we compute the total SN energy that will be deposited based on the Chabrier IMF, and assign 30% (70%) of that energy to gas particles within the shock radius as the kinetic (thermal) energy. The metals are also distributed in the same manner as the SN energy.

2.3 Mock data for future observations

In order to compare the two simulations on the same ground, we first define a 512^3 grid in the simulation box to recompute the H I density field, where each grid-cell size is $146.5 h^{-1} \text{kpc}$ for Illustris and $166.0 h^{-1} \text{kpc}$ for Osaka simulation, respectively. These grid scales are much finer than the scale of our interest, therefore it will not affect our conclusion on the large-scale bias. The density field is represented by the SPH particles (or the fluid element in the Voronoi cells for the Illustris simulation) which have corresponding density and smoothing scale. For the Osaka simulation, we use

the density and the smoothing scale of each SPH particle, and recompute the H I density field on our grid using the following cubic spline kernel (Monaghan & Lattanzio 1985):

$$W^{\text{SPH}}(r; h) = A \begin{cases} 1 - \frac{3}{2} \left(\frac{r}{h/2} \right)^2 + \frac{3}{4} \left(\frac{r}{h/2} \right)^3 & 0 < r < \frac{h}{2} \\ \frac{1}{4} \left(2 - \frac{r}{h/2} \right)^3 & \frac{h}{2} < r < h \\ 0 & h < r \end{cases}, \quad (2)$$

where h is the smoothing length for each particle, and r is the distance between the particle and the grid. The amplitude A is determined such that for every particle, the sum of W^{SPH} over all grid becomes unity.

For the Illustris simulation, we define the smoothing length of each fluid element as

$$h = 2 \left(\frac{3V}{4\pi} \right)^{\frac{1}{3}}, \quad (3)$$

where V is the volume of each Voronoi cell. We checked that the above methods give similar PDFs of H I density in both simulations. Using this smoothing length and Eq. (2), we compute the H I density in each grid-cell similarly to the Osaka simulation.

The H I gas density in each grid is then calculated by summing over all contributing particles,

$$\rho_{\text{H I}}^{\text{SPH}}(\mathbf{x}_i) = \sum_j W^{\text{SPH}}(|\mathbf{x}_i - \mathbf{x}_j|; h_j) \rho_j n_{\text{H I},j}, \quad (4)$$

where ρ_j and $n_{\text{H I},j}$ denote the total gas density and neutral hydrogen fraction assigned to the j -th particle located at \mathbf{x}_j in the simulation box. For the particle which has too small smoothing scale at high-density region, the mass is deposited only to the local cell. Figure 1 shows the H I density contrast $1 + \delta = \rho/\bar{\rho}$ in logarithmic scales from the two simulations, where $\bar{\rho}$ is the mean density at each redshift. The obtained density contrast of H I defined on the regular grid is Fourier transformed using the python module `numpy.fft`, and we obtain the three dimensional density field in Fourier space. We note that the different scheme to define the gas density with adaptive mesh refinement can be found in Behrens et al. (2018).

Here we further consider the angular and frequency resolutions for the *Square Kilometer Array* (SKA)-like observation for both interferometer and single-dish observations. For other future observations, we can redefine the resolution of the grid according to the specification of each observation. For the interferometer mode, the angular resolution is quite high, and we assume here that the H I cloud is identified at the resolution of $3'$, which corresponds to the comoving scale of $2 h^{-1} \text{Mpc}$ at $z = 1$ and $4.8 h^{-1} \text{Mpc}$ at $z = 5$, respectively. However, the field of view of interferometer is small and not optimal for a large sky coverage. On the other side, the single dish observation has a wide field of view, but the angular resolution is relatively coarse. For single-dish observations, given that the size of dish is fixed, we assume that the angular resolution is proportional to the observed wavelength as $\theta = \lambda_{\text{obs}}/D$, where λ_{obs} is the observed wavelength of 21 cm line and D is the diameter of the dish, $D = 15$ meters for SKA. This corresponds to the angular size of $48.1(1 + z_{\text{H I}})$ arcmin, which is comoving $65 h^{-1} \text{Mpc}$ at $z = 1$ and $460 h^{-1} \text{Mpc}$ at $z = 5$, respectively. The spatial resolution along the line of sight (LoS) is determined by the frequency resolution of the observation. We assume 50 kHz for all frequency channels which is much finer than our initial choice of the grid. Thus we do not redefine the radial resolution.

² <https://grackle.readthedocs.org/>

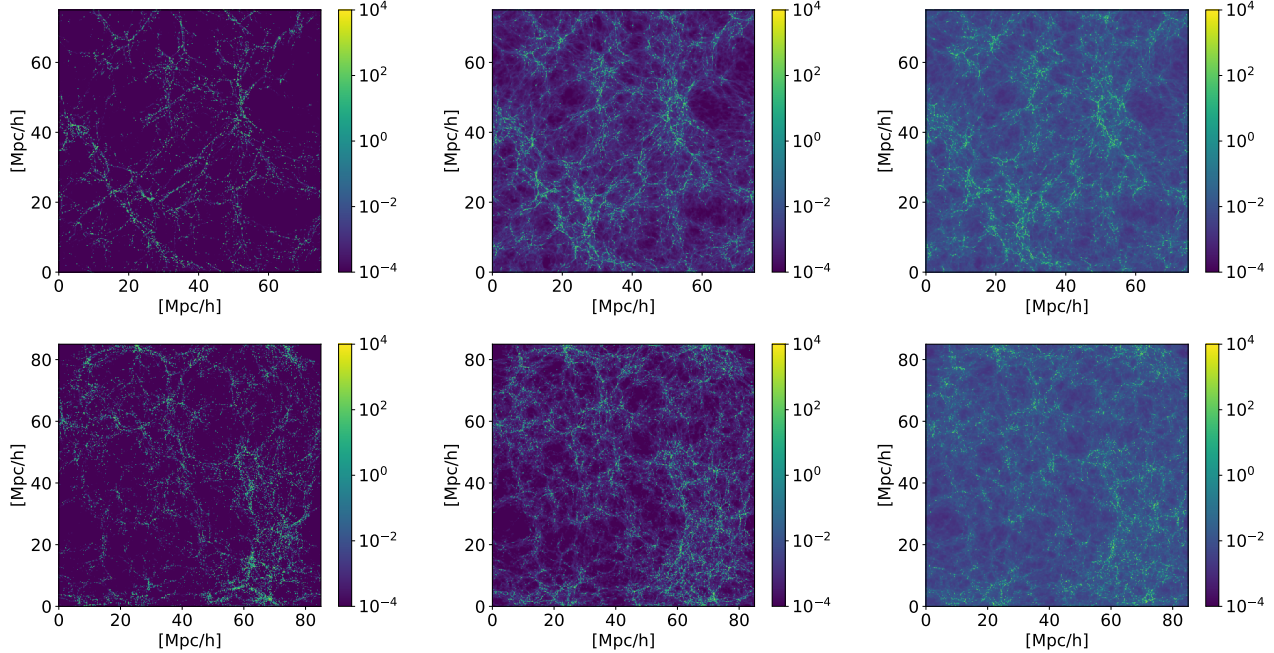


Figure 1. Hi gas distribution at redshift $z = 1, 3$ and 5 from left to right panels, for Illustris simulation (upper panels) and Osaka simulation (lower panels). Color gradient represents the Hi gas overdensity $1 + \delta = \rho_{\text{Hi}}/\bar{\rho}_{\text{Hi}}$ in logarithmic units, where $\bar{\rho}_{\text{Hi}}$ is the mean Hi density at each redshift.

3 SCALE DEPENDENT BIAS IN REAL SPACE

For the unbiased measurement of the dark energy parameters through the location of BAO peaks and troughs, it is important to understand the scale dependences of bias of Hi gas on large scales where the matter clustering is in quasi-linear regime. In this section, we first measure the Hi power spectrum and evaluate the significance of scale dependence of Hi clustering without considering the redshift space distortion. The effect of RSD will be considered in Section 4.

3.1 Measurement of Power Spectrum and Hi bias

As we only work with the simulation data, it is useful to work in the Fourier space. Thus we define the Hi bias using the power spectrum. In real space, where we do not consider the RSD effect, only the absolute value of wavenumber is considered from $k_{\min} = 2\pi/L_{\text{box}}$ to $k_{\max} = \pi N_{\text{grid}}/L_{\text{box}}$. The power spectrum is then calculated as the algebraic mean among the absolute value of k ,

$$P_{XY}(k_i) = \frac{1}{N_k} \sum_{j, k_j \in k_i} \Re[\delta_X(k_j)\delta_Y^*(k_j)], \quad (5)$$

where X, Y denote either total matter or Hi density fluctuation. The Hi bias can then be defined using the measured power spectra as

$$\hat{b}_{\text{Hi}}^{\text{cross}}(k) \equiv \frac{P_{\text{Hi},m}(k)}{P_m(k)}, \quad (6)$$

where $P_{\text{Hi},m}$ and P_m are the power spectra of Hi–matter cross correlation and matter auto correlation, respectively. Note that the matter is a sum of dark matter and gas components in the simulation. Another way of defining the Hi bias would be

$$\hat{b}_{\text{Hi}}^{\text{auto}}(k) \equiv \sqrt{\frac{P_{\text{Hi}}(k) - S}{P_m(k)}}, \quad (7)$$

where P_{Hi} is the auto power spectrum of Hi gas, and S is the corresponding shot-noise. The two different definitions of bias are identical on large scales where the density fluctuation is described by the linear perturbation theory and the effect of shot-noise is not dominant. In the language of higher order perturbation theory, on the quasi-linear scales, the mode coupling between different wavenumber modes enters differently for cross-correlation and auto-correlation for the biased tracers. This makes the different definitions of bias behave differently. In this paper, we take the former definition, because the shot-noise of Hi gas is not well-defined in the simulation and the cross correlation is totally free from the shot-noise effect. Hereafter we write $\hat{b}_{\text{Hi}} \equiv \hat{b}_{\text{Hi}}^{\text{cross}}$ for simplicity.

Figure 2 shows the measured Hi bias using the Illustris and the Osaka simulations. Due to the limited box-size of the simulations, we cannot go to the larger scale of $k < 0.1 h\text{Mpc}^{-1}$, however, the plot clearly shows that the Hi bias seems to converge to a constant value on large scales. The constant convergent value depends largely on the redshift, and we see that the bias is higher at higher redshifts. We will discuss in the next section in more detail, but the Illustris simulation has systematically lower values of bias compared to those in the Osaka simulation at all redshift ranges.

At $1 < z < 3$, since the Universe is almost perfectly ionized (Fan et al. 2006; Becker et al. 2015) and the amount of the neutral hydrogen in the IGM is negligibly small, the majority of Hi gas is confined in the high-density regions such as inside the galactic halos (e.g. Nagamine et al. 2004a,b). Nevertheless, compared to the bias of QSOs, the Hi bias is still lower (e.g. Laurent et al. 2017). This implies that the Hi gas is more broadly distributed than QSOs, or in other words, the QSOs reside only in extremely high-density environment.

3.2 Scale dependence of Hi bias

It is known that the scale dependence of bias may shift the scale of BAO peak, and therefore, an accurate modeling is crucial for pre-

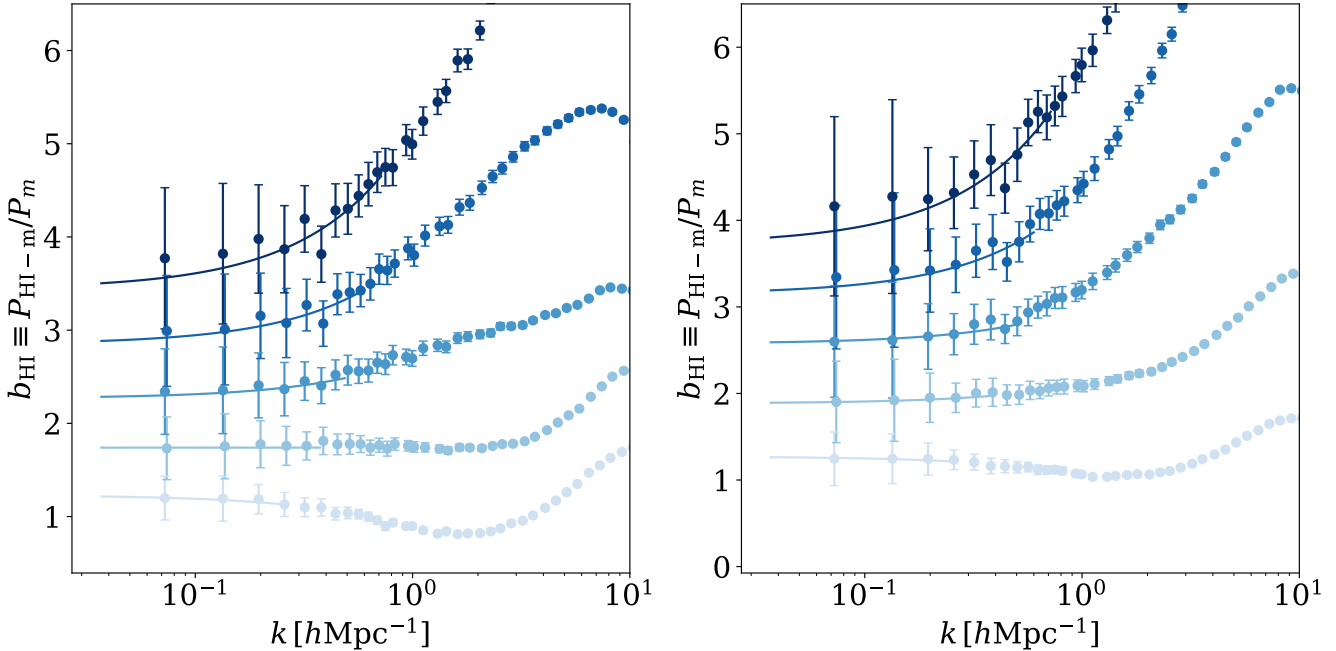


Figure 2. H_I bias defined by the cross correlation (Eq. 6) measured from the Illustris simulation (*left*) and the Osaka simulation (*right*). In both panels, the lines correspond to $z = 5, 4, 3, 2,$ and 1 from top to bottom, respectively. The solid curves are the best-fitting models defined by Eq. (8). The error bars are shifted slightly for illustrative purposes.

cisely constraining the cosmological parameters. To find the signature of scale dependence of H_I bias, here we introduce the linear function of k as

$$b_{\text{HI}}(k) = b_0 + b_1 k, \quad (8)$$

where b_0 and b_1 are free parameters. We fit the measured H_I bias from simulations with Eq.(8) to quantify the scale dependence.

We find the best-fitting parameters by a usual Metropolitan-Hastings MC method with the likelihood

$$\mathcal{L} = \exp \left[-\frac{1}{2} \sum_i^{k_i < k_{\text{max}}} \frac{(\hat{b}_{\text{HI},i} - b_{\text{HI}}(k_i))^2}{\sigma_i^2} \right], \quad (9)$$

where k_{max} is the maximum wavenumber for the fitting. We first choose k_{max} so that the fluctuation of dark matter is not too large,

$$\frac{k_{\text{max}}^2}{6\pi^2} \int_0^{k_{\text{max}}} dk P^{\text{lin}}(k, z) = C, \quad (10)$$

with C being 0.7. This criterion is empirically derived, such that the dark matter power spectrum of N -body simulation and prediction of higher-order perturbation theory agrees within 1% (Nishimichi et al. 2009; Taruya et al. 2009). This is slightly conservative for our study, but it reasonably suggests the scale where the structure becomes quasi-linear and the H_I bias supposedly having a scale dependence. Figure 3 shows the best-fitting parameters for the H_I bias. As one can see, both the constant bias and scale dependent component are consistent between two different simulations. We find that the scale dependence of H_I bias at $z < 3$ is insignificant and consistent with constant bias. On the other hand, at $z > 3$, we find a significant scale dependence of the bias. We emphasize that the scale dependence of H_I bias is independent from the details of astrophysical effects which are different in two distinct simulations. We will further discuss this point in Section 5.1.

4 H_I POWER SPECTRUM IN REDSHIFT SPACE

4.1 Anisotropic Power Spectrum in Redshift Space

When we measure the cosmological distance to an object, we use the redshift which can be decomposed into cosmological recession velocity and local peculiar velocity of the object. In a limit of Cartesian coordinate, the position of the object can be written as

$$(s_1, s_2, s_3) = \left(\chi_1, \chi_2, \chi_3 + \frac{v}{aH} \right), \quad (11)$$

where s_i and χ_i ($i = 1, 2, 3$) are the comoving distance in redshift space and real space, respectively. The coordinate along the line-of-sight (LoS) is $i = 3$. The modification to the distance due to the peculiar velocity affects only the separation of two objects along the LoS, which makes the two dimensional correlation function or power spectrum in redshift space distorted (Kaiser 1987) in addition to the geometrical distortion (Matsubara 2004).

The Osaka simulation uses the SPH method for hydrodynamics, and the gas density and neutral hydrogen fraction is represented by each gas particle. Thus we can map the real space density distribution to that in the redshift space simply by moving the gas particle along the LoS direction by v_3/aH . The grid based density can then be computed in the exactly same manner described in Section 2.3.

Figure 4 shows the 2D H_I power spectra $P(k_{\parallel}, k_{\perp})$ in redshift space and real space. We see that the $P(k_{\parallel}, k_{\perp})$ is elongated along the LoS direction. While the elongation is more significant on larger scales due to the Kaiser effect, on smaller scales, the power spectrum shrinks in redshift space, which is caused by the non-linear velocities. The transition from elongation to squashing occurs at $k \approx 1 \text{ hMpc}^{-1}$. Figure 4 also shows the spectra with an angular resolution of SKA-like observation in the interferometer and the single-dish observation modes. Since the single-dish observation has low angular resolution, the small-scale fluctuations in the

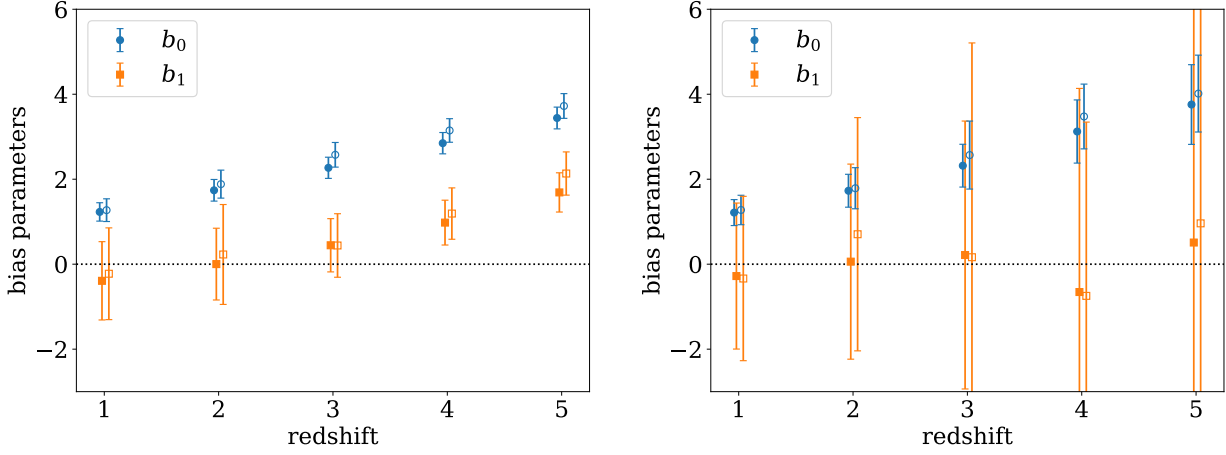


Figure 3. *Left panel:* Best-fitting H_I bias parameters for Illustris (filled) and Osaka (open) simulations. The value of k_{\max} used for the fitting is given by the limit defined in Eq. (10). The bias parameters are consistent with each other in the two simulations, and we clearly find the scale dependence only at $z > 3$ while it is consistent with being constant (i.e. $b_1 = 0$) at $z < 3$. The data points are slightly shifted horizontally for illustrative purposes. *Right panel:* Same as the left panel but for $k_{\max} = 0.25 \text{ hMpc}^{-1}$. The bias is consistent with being constant at all redshift ranges.

transverse direction are considerably smoothed out. Conversely, the power spectrum for the interferometer map has a negligible effect of smoothing.

4.2 RSD model, Kaiser Effect, and Fingers of God

In this section, we describe the theoretical models for the anisotropic power spectrum of the H_I gas distribution in redshift space. H_I gas traced by 21cm line is also affected by the peculiar motion of the gas clouds exactly in the same way as the galaxy doppler shift. In the limit of linear theory for the velocity, Kaiser formula gives

$$P_{\text{H}_I}^{(s),\text{Kaiser}}(k, \mu) = b_{\text{H}_I}^2 (1 + \beta \mu^2)^2 P_{\text{dm}}^{\text{lin}}(k), \quad (12)$$

where μ is cosine of the angle between LoS and wavenumber vector \mathbf{k} , b_{H_I} is the H_I bias, which we assume to be constant at first, and $\beta = f/b$ is the linear growth rate divided by the bias. Phenomenologically, the Fingers-of-God effect can be included as

$$P_{\text{H}_I}^{(s)}(k, \mu) = \text{DFoG}[k\mu f\sigma_v] P_{\text{H}_I}^{(s),\text{Kaiser}}(k, \mu), \quad (13)$$

where the prefactor DFoG represents the effect of damping given by either Gaussian or Lorentzian function in the literature,

$$\text{DFoG}[x] = \begin{cases} \exp(-x^2) & \text{Gaussian} \\ \frac{1}{1+x^2} & \text{Lorentzian.} \end{cases} \quad (14)$$

The velocity dispersion σ_v can be given by either linear theory or just treated as free parameters later on. If we focus on smaller scales, we may need to model the non-linearity of the density and velocity fields, which can be given as

$$P_{\text{H}_I}^{(s),\text{Kaiser}}(k, \mu) = b^2 \left(P_{\delta\delta}(k) + 2\beta\mu^2 P_{\delta\theta}(k) + \beta^2\mu^4 P_{\theta\theta}(k) \right), \quad (15)$$

where θ represents the divergence of velocity for H_I gas and we assume no velocity bias. Here $P_{\delta\delta} = P_{\text{dm}}$ is the dark matter power spectrum, $P_{\theta\theta}$ is velocity divergence power spectrum and $P_{\delta\theta}$ is the cross-power spectrum. Note that Eq. (15) is reduced to Eq. (12) in the limit of linear theory. For further non-linear correction, we consider the additional terms in Taruya et al. (2010):

$$P_{\text{H}_I}^{(s)}(k, \mu) = \text{DFoG}[k\mu f\sigma_v] \left(P_{\text{H}_I}^{(s),\text{Kaiser}}(k, \mu) + b_{\text{H}_I}^3 A(k, \mu) + b_{\text{H}_I}^4 B(k, \mu) \right), \quad (16)$$

where A and B terms are introduced so that the modulation of BAO is readily accounted for at relatively large scales in quasi-nonlinear regimes. In this paper, we compute $P_{\text{H}_I}^{(s),\text{Kaiser}}$ using a publicly available code, RegPT (Taruya et al. 2012) up to 2-loop order for $P_{\delta\delta}$, $P_{\delta\theta}$ and $P_{\theta\theta}$. As an alternative model, we replace the linear power spectrum in Eq. (12) with the full non-linear power spectrum $P^{\text{NL}}(k)$, obtained by the fitting formula by Takahashi et al. (2012). Furthermore, we consider the angular resolution of the intensity mapping survey in the anisotropic power spectra. Since the density fluctuations on the direction perpendicular to the line-of-sight are observed convolved with the antenna beam function, the observed anisotropic power spectrum can be written as

$$P_{\text{H}_I,\text{obs}}^{(s)}(k, \mu) = W_{\text{beam}}^2(k, \mu) P_{\text{H}_I}^{(s)}(k, \mu), \quad (17)$$

where we assume that W_{beam} is Gaussian function

$$W_{\text{beam}} = \exp\left(-\frac{k^2(1-\mu^2)\sigma_{\text{smooth}}^2}{2}\right). \quad (18)$$

σ_{smooth} is the comoving scale corresponding to the angular resolution at observed 21 cm redshift.

In order to compare the model with the simulation results, it is useful to expand the anisotropic power spectrum in a Legendre polynomial series,

$$P_l^{(s)}(k) = \frac{2l+1}{2} \int_{-1}^1 d\mu P^{(s)}(k, \mu) \mathcal{L}_l(\mu), \quad (19)$$

where $l = 0, 2$ or 4 , and \mathcal{L}_l is the l -th Legendre polynomial.

For the simulation data, we calculate the multipole H_I power spectra $P_l^{(s)}(k)$ as,

$$\hat{P}_l^{(s)}(k_i) = \frac{2l+1}{2} \sum_{j,k_j \in k_i} \Re[\delta_{\text{H}_I}(k_j) \delta_{\text{H}_I}^*(k_j)] \mathcal{L}_l(\mu_j) \Delta\mu_k, \quad (20)$$

where $\mu = k_{\parallel}/k$, $\Delta\mu_k = 2/N_k$ and N_k is the number of modes within the j -th wavenumber bin. We then find the best-fitting parameters with the following likelihood:

$$\mathcal{L} \propto \exp\left(-\frac{\chi_{l=0}^2 + \chi_{l=2}^2}{2}\right), \quad (21)$$

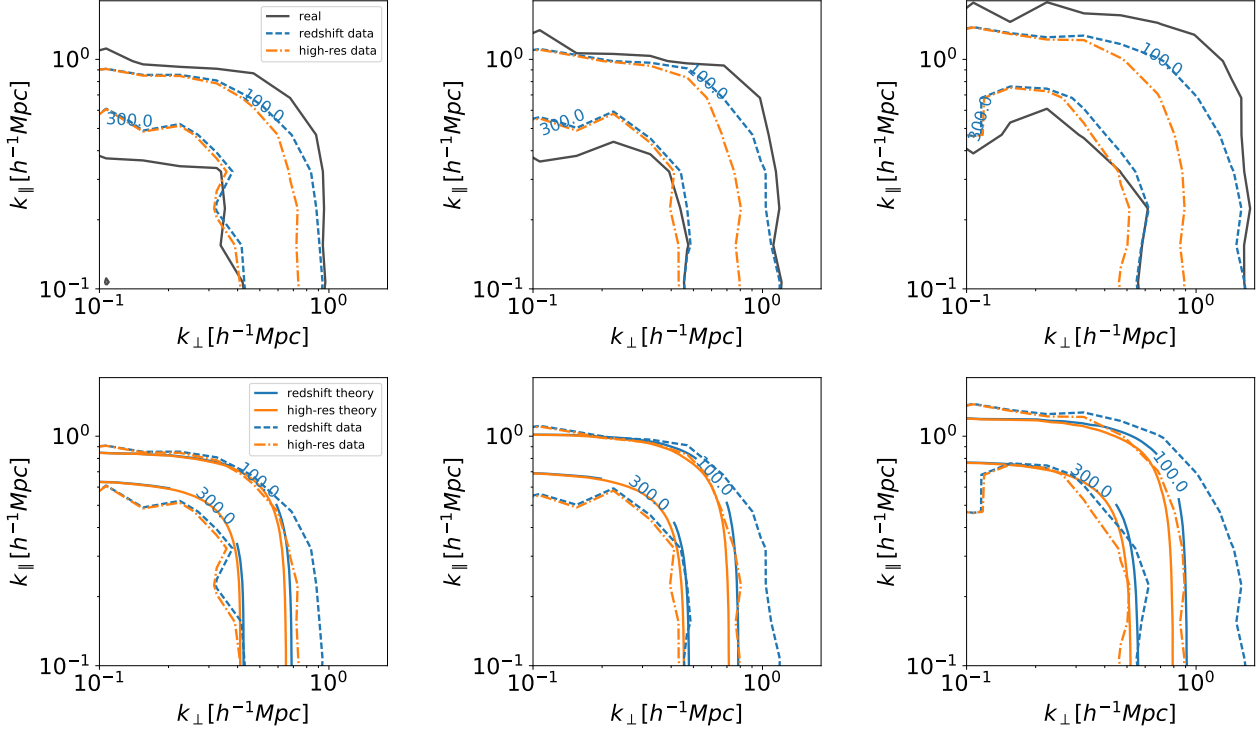


Figure 4. Two dimensional power spectra of the H I gas density, $P(k_{\perp}, k_{\parallel})$ at $z=3, 4$, and 5 from left to right, measured from the Osaka simulation. The abscissa and ordinate are the wave numbers perpendicular and parallel to the LoS. The upper panels compare the power spectra in the real and redshift space, which are expected to be observed with different angular resolutions. Comparing spectra in real space with the one in redshift space, one can see that the spectra is elongated along the LoS due to the Kaiser effect, while on small scales the FoG effect is more prominent and the spectra are squashed. Lower panels compare the simulated results with the theoretical predictions given by the TNS model with the best-fitting parameters given in Tables 1 and 2.

where χ_l is the chi-square for the l -th moment,

$$\chi_l^2 = \sum_i^{k_i < k_{\max}} \frac{[\hat{P}_{l,i}^{(s)} - P_l^{(s)}(k_i)]^2}{\sigma_i^2}. \quad (22)$$

We fit the results with three models for $0.18 < k < k_{\max}$. We set the linear H I bias b_0 and velocity dispersion σ_v (see Eq. (13)) as free parameters and fit within the range of $0.1 \leq b_0 \leq 5$ and $0 \leq \sigma_v \leq 5 \sigma_{\text{lin}}$, where σ_{lin} is the velocity dispersion predicted from the linear perturbation theory. As we only use the single realisation of simulation, the large-scale fluctuation is highly affected by the cosmic variance. We find that the dark matter power spectra at $k < 0.18 h\text{Mpc}^{-1}$ of our simulation has significantly smaller amplitude compared to the theoretical prediction of the matter power spectrum and thus a lower H I bias is favoured. (Note that the wave number corresponding to the box-size is $k_{\min} = 2\pi/L_{\text{box}} = 0.074 h^{-1}\text{Mpc}$.) Therefore we decide to remove the two largest modes from the fitting. Note that the bias measurement in Eq. (6) does not suffer from this effect because the amplitude suppression appear both in dark matter and H I and they are cancelled out. The maximum wavenumber k_{\max} is again given by Eq. (10).

Figure 5 compares the measured power spectra and the following models with best-fitting parameters: linear model (Eqs. (12) & (13)), alternative model (i.e. the linear power spectrum $P_{\text{dm}}^{\text{lin}}(k)$ in Eq. (12) is replaced with the non-linear power spectrum), and TNS model (Eq. (16)). We find that the alternative model and the TNS model agree well with the measured H I power spectra. The chi-square values ($\chi_0^2 + \chi_2^2$) for the linear model, alternative model, and TNS model are 28, 17, and 17, respectively; that is, the fitting by the alternative model and TNS model are improved by $\Delta\chi^2 = 12$,

suggesting that these two models are better than the linear model. Since $P_{\text{dm}}^{\text{lin}}(k)$ in Eq. (12) is simply derived from the linear theory, the linear model does not fully consider the non-linearity. Therefore the best-fitting value of velocity dispersion σ_v for the linear model is smaller than others. The best-fitting parameters for each model are shown in Tables 1 and 2.

5 IMPLICATIONS

In this section, we compare the H I biases measured from the real space power spectra between Illustris and Osaka simulations which are based on different prescriptions of astrophysical effects. We also discuss the bias and velocity dispersion parameters derived from the redshift space observation to understand the H I clustering properties.

5.1 Comparison between Illustris and Osaka simulations

Here we compare the two different simulations in terms of H I bias behaviour. On large scales, the overall behaviour of the two simulations is similar to each other. Although the two simulations have different astrophysical effects as described in Section 2, those effects are only seen on small scales and on larger scales of $k < k_{\max}$ defined in Eq. (10), the effects do not significantly affect the values of H I bias both for constant and scale dependent terms. This suggests that details of the astrophysical effects in the simulation are not important for measuring the scale dependent bias and that the

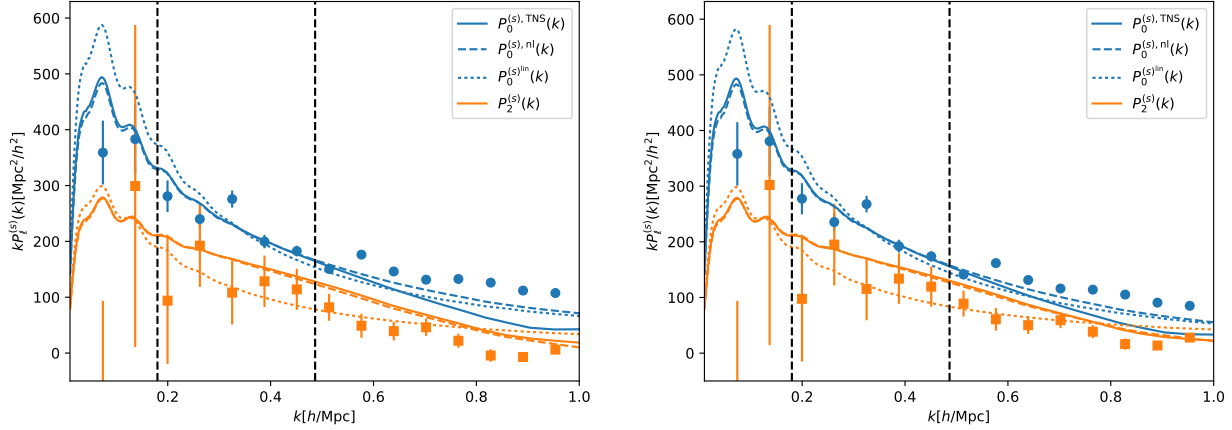


Figure 5. *Left panel:* Legendre expansion of anisotropic power spectra assuming the angular resolution of single-dish mode. The blue upper set of lines and symbols are monopole, and orange lower set of lines are quadrupole. Symbols are measured from the Osaka simulation, and the curves are the best-fitting models for $0.18 < k < k_{\max}$, using the TNS (solid), non-linear empirical (dashed) and linear theory (dotted), respectively. The vertical dashed line shows the scale of 0.18 and k_{\max} . *Right panel:* Same as the left panel, but with the angular resolution assuming the interferometer mode.

future analysis of measuring the BAO scales are robust against the baryonic effects.

5.2 Bias and velocity dispersion

In this section, we explore the linear bias and velocity dispersion parameters (see Eq. (13)) simultaneously fitted to the redshift space power spectra, keeping the cosmological parameters fixed to the values used in the simulations. The detailed procedure of estimating the best-fitting parameters are described in Section 4.2.

Figure 6 shows the redshift dependence of bias and velocity dispersion of HI gas obtained by fitting the Legendre polynomial expanded data with the TNS model. The best-fitting models are compared with the real space measurement of the bias or the prediction from linear perturbation theory for the velocity dispersion. In the top panel, we find that the constant bias is systematically smaller than that obtained by the direct measurement using Eq. (8). With a low angular resolution, the bias is significantly underestimated though it is still consistent with the direct measurement within $1-\sigma$ error. In the bottom panel of Fig. 6, we find that the velocity dispersion of HI gas is marginally consistent with the linear theory prediction at $z \sim 1$, but it is systematically smaller than the linear theory at $z > 2$, although the uncertainties are still large.

Since the angular resolution of single-dish mode is comparable or worse than the box-size of our simulation, it is infeasible to estimate the two dimensional anisotropic power spectrum because the transverse fluctuation is fully smoothed out. Thus we can not measure the bias parameters for single-dish mode and need simulations with larger box-size. Both bias and velocity dispersion are underestimated even for the no-smooth case, and we need to develop in the future a more sophisticated model for the non-linear HI power spectra which takes the coarse angular resolution into account.

6 SUMMARY AND CONCLUSIONS

Future 21 cm surveys will reveal the three dimensional distribution of neutral hydrogen gas over cosmological scales, which will potentially be a new probe of the large-scale structure of the Universe.

In this paper, we explore the properties of HI clustering using two different set of cosmological hydrodynamic simulations, the Illustris and the Osaka simulations that include the nonlinear baryonic effects of star formation and feedback.

We first measure the scale and redshift dependences of HI bias in real space by taking the ratio of power spectra of HI–dark matter cross correlation and dark matter auto correlation. Fitting with the constant plus linearly scaled bias with k , we find that the HI bias shows a significant scale dependence at $z > 4$ up to the scales where the perturbation theory holds, but it is consistent with being constant at $z \leq 3$. If we limit our analysis to the large scales of $k < 0.25 \text{ hMpc}^{-1}$, we find no evidence of scale dependence at $1 < z < 5$. In both cases, the best-fitting bias parameters are fairly consistent between Illustris and Osaka simulations, which implies that the scale dependence of HI bias on large scales is not sensitive to the details of the small-scale astrophysics. This means that, as far as we use the large scale modes, the cosmological analysis such as the determination of BAO scale is unlikely to be affected by the astrophysical uncertainties of feedback on small scales. However, at the same time, if one use the data more aggressively up to higher k , we certainly need accurate knowledge on the astrophysical effects such as supernova or AGN feedback. We leave more detailed and thorough investigation of the astrophysical impact of feedback on the HI power spectrum as a future work.

We then measure the redshift space distortion using the anisotropic two dimensional power spectrum. We jointly fit the monopole and quadrupole of the Legendre expanded power spectra including the peculiar velocity effect to the models widely applied for galaxy redshift surveys, with the free parameters of bias b_{HI} and velocity dispersion σ_v . We note that, since we only have two simulations, the cosmic variance largely affects the amplitude of large scale fluctuations. Therefore, we fit the data only in the range of $0.18 < k < k_{\max}$ where k_{\max} is given by Eq. (10). We find that the measured bias parameter in redshift space is consistent with the one directly measured in real space from the ratio of power spectra. We also find that the velocity dispersion of HI gas is systematically below the prediction from linear perturbation theory but marginally consistent with the prediction.

Compared with the previous work by Sarkar & Bharadwaj (2018), we find significant disagreement on the values of HI bias

redshift	TNS	TNS	non-linear	non-linear	linear	linear
	no smooth	high res.	no smooth	high res.	no smooth	high res.
1	1.07 ^{+0.07} _{-0.10}	1.07 ^{+0.07} _{-0.10}	1.03 ^{+0.07} _{-0.10}	1.03 ^{+0.07} _{-0.10}	1.12 ^{+0.07} _{-0.07}	1.12 ^{+0.07} _{-0.07}
2	1.65 ^{+0.07} _{-0.05}	1.64 ^{+0.08} _{-0.04}	1.61 ^{+0.06} _{-0.07}	1.60 ^{+0.07} _{-0.06}	1.85 ^{+0.06} _{-0.03}	1.85 ^{+0.06} _{-0.04}
3	2.43 ^{+0.06} _{-0.05}	2.43 ^{+0.05} _{-0.06}	2.39 ^{+0.06} _{-0.06}	2.39 ^{+0.05} _{-0.07}	2.69 ^{+0.05} _{-0.04}	2.68 ^{+0.05} _{-0.04}
4	3.47 ^{+0.06} _{-0.04}	3.45 ^{+0.06} _{-0.04}	3.45 ^{+0.05} _{-0.06}	3.42 ^{+0.05} _{-0.06}	3.82 ^{+0.04} _{-0.04}	3.79 ^{+0.05} _{-0.03}
5	4.93 ^{+0.05} _{-0.03}	4.88 ^{+0.04} _{-0.04}	4.90 ^{+0.04} _{-0.04}	4.83 ^{+0.05} _{-0.03}	5.35 ^{+0.05} _{-0.04}	5.32 ^{+0.04} _{-0.05}

Table 1. Best-fitting parameters for the constant bias b_{HI} in the non-smoothed case and high-angular resolution case. Superscript and subscript are upper and lower 68 percentiles.

redshift	TNS	TNS	non-linear	non-linear	linear	linear
	no smooth	high res.	no smooth	high res.	no smooth	high res.
1	3.66 ^{+0.67} _{-1.01}	3.71 ^{+0.62} _{-1.05}	3.96 ^{+0.61} _{-0.88}	3.96 ^{+0.60} _{-0.89}	2.02 ^{+0.89} _{-1.38}	2.02 ^{+0.89} _{-1.38}
2	0.98 ^{+0.68} _{-0.65}	0.86 ^{+0.79} _{-0.54}	1.30 ^{+0.52} _{-0.89}	1.24 ^{+0.56} _{-0.84}	0.00 ^{+0.97}	0.00 ^{+0.97}
3	0.67 ^{+0.35} _{-0.45}	0.72 ^{+0.30} _{-0.50}	0.87 ^{+0.27} _{-0.57}	0.90 ^{+0.24} _{-0.60}	0.00 ^{+0.49}	0.00 ^{+0.49}
4	0.40 ^{+0.25} _{-0.26}	0.38 ^{+0.24} _{-0.26}	0.56 ^{+0.17} _{-0.37}	0.54 ^{+0.16} _{-0.37}	0.00 ^{+0.26}	0.00 ^{+0.26}
5	0.00 ^{+0.20}	0.00 ^{+0.19}	0.00 ^{+0.21}	0.00 ^{+0.20}	0.00 ^{+0.13}	0.00 ^{+0.13}

Table 2. Same as Table 1 but for σ_p parameter.

for the entire redshift range, which may mainly arise from the prescription of the H I gas assignment to the dark matter halos in an N -body simulation by Sarkar & Bharadwaj (2018). On the other hand, the best-fitting values of our velocity dispersion are fairly consistent with the previous work within the statistical error of the single box simulation. Although the simulations used in this paper solve baryonic distribution and hydrogen ionization process in a more realistic manner, more detailed analysis will be required to fully understand the discrepancy.

In this paper, we also introduced a new empirical model for RSD. The model is a simple replacement of linear power spectrum $P^{\text{lin}}(k) \rightarrow P^{\text{NL}}(k)$ in the Kaiser formula with the FoG prefactor. This model is consistent with the full TNS model on scales $k < k_{\text{max}}$, and it gives a better fit of monopole at $k > k_{\text{max}}$ but slightly off from the data for quadrupole on those scales.

We construct a mock simulated data assuming that the 21 cm line is observed by future SKA-like survey for both interferometer and single-dish modes. We find that, for single-dish observation (i.e. low angular resolution observation), the models systematically underestimate the bias parameter and velocity dispersion. It will require a model in which the coarse angular resolution has been taken into account.

In this paper we have limited ourselves to the discussion of the clustering properties of H I gas, however it is straightforward to extend our analysis to the cosmological parameter recovery, such as the growth rate f or dark energy parameters w or Ω_{DE} . We leave these analysis to our future work, in which we will employ a larger number of hydrodynamic simulations with larger box-sizes.

ACKNOWLEDGMENTS

We would like to thank Drs. Naoshi Sugiyama, Hiroyuki Tashiro, Atsushi Taruya and Fabian Schmidt for useful discussions. AN is in part supported by JSPS KAKENHI Grant Number JP16H01096. KH is in part supported by JSPS KAKENHI Grant Numbers JP17H01110 and JP18K03699. IS and KN acknowledge the support by the JSPS KAKENHI Grant Number JP17H01111. The Os-

aka simulations were performed on Cray XC30 at CfCA, National Astronomical Observatory of Japan, as well as the OCTOPUS at the Cyber Media Centre, Osaka University.

REFERENCES

- Alam S. et al., 2017, MNRAS, 470, 2617
 Albrecht A. et al., 2006, ArXiv Astrophysics e-prints
 Alcock C., Paczynski B., 1979, Nature, 281, 358
 Aoyama S., Hou K.-C., Shimizu I., Hirashita H., Todoroki K., Choi J.-H., Nagamine K., 2017, MNRAS, 466, 105
 Battye R. A. et al., 2012, ArXiv e-prints
 Becker G. D., Bolton J. S., Madau P., Pettini M., Ryan-Weber E. V., Venemans B. P., 2015, MNRAS, 447, 3402
 Behrens C., Byrohl C., Saito S., Niemeyer J. C., 2018, Astronomy & Astrophysics, 614, A31
 Beutler F. et al., 2011, MNRAS, 416, 3017
 Bowman J. D., Rogers A. E. E., Monsalve R. A., Mozdzen T. J., Mahesh N., 2018, Nature, 555, 67
 Bull P., Ferreira P. G., Patel P., Santos M. G., 2015, ApJ, 803, 21
 Busca N. G. et al., 2013, Astronomy & Astrophysics, 552, A96
 Camera S., Santos M. G., Maartens R., 2015, MNRAS, 448, 1035
 Clifton T., Ferreira P. G., Padilla A., Skordis C., 2012, Phys.Rep., 513, 1
 Cole S. et al., 2005, MNRAS, 362, 505
 Dalal N., Doré O., Huterer D., Shirokov A., 2008, Phys. Rev. D, 77, 123514
 de la Torre S. et al., 2017, Astronomy & Astrophysics, 608, A44
 Dinda B. R., Sen A. A., Choudhury T. R., 2018, ArXiv e-prints
 Eisenstein D. J. et al., 2005, ApJ, 633, 560
 Fan X. et al., 2006, AJ, 132, 117
 Faucher-Giguère C.-A., Lidz A., Zaldarriaga M., Hernquist L., 2009, ApJ, 703, 1416
 Genel S. et al., 2014, MNRAS, 445, 175
 Haardt F., Madau P., 2012, ApJ, 746, 125
 Haider M., Steinhauser D., Vogelsberger M., Genel S., Springel V., Torrey P., Hernquist L., 2016, MNRAS, 457, 3024

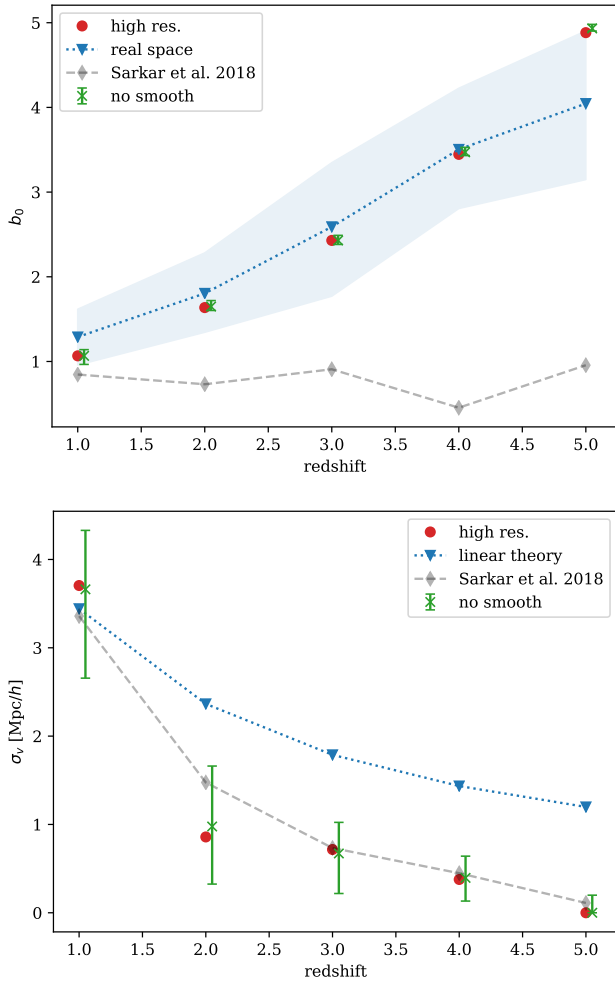


Figure 6. (*Top:*) Best-fitting values of b_{HI} and those obtained for the real space power spectrum b_0 defined in Eq. (8) (dotted-line and triangle symbols). The shaded region is a 1-sigma uncertainty on b_0 . (*Bottom:*) Best-fitting values of σ_v compared with that predicted from linear perturbation theory (dashed-line with triangle symbol). For both panels, the crosses with error bars and the red circle symbols correspond to the fitting results with the TNS model to the non-smoothed and high-angular resolution data, respectively. For both panels, also shown with dashed line is the best-fitting model of B1 (HC) of Sarkar & Bharadwaj (2018).

Hamilton A. J. S., 1998, in *Astrophysics and Space Science Library*, Vol. 231, *The Evolving Universe*, Hamilton D., ed., p. 185
 Hinshaw G. et al., 2013, *ApJS*, 208, 19
 Kaiser N., 1987, *MNRAS*, 227, 1
 Kirshner R. P., Oemler, A. J., Schechter P. L., Sheckman S. A., 1981, *ApJ*, 248, L57
 Laurent P. et al., 2017, *JCAP*, 7, 017
 Matsubara T., 2004, *ApJ*, 615, 573
 McDonald P., Roy A., 2009, *JCAP*, 8, 020
 Monaghan J. J., Lattanzio J. C., 1985, *Astronomy & Astrophysics*, 149, 135
 Nagamine K., Springel V., Hernquist L., 2004a, *MNRAS*, 348, 421
 Nagamine K., Springel V., Hernquist L., 2004b, *MNRAS*, 348, 435
 Nelson D. et al., 2015, *Astronomy and Computing*, 13, 12
 Nishimichi T. et al., 2007, *PASJ*, 59, 1049

Nishimichi T. et al., 2009, *PASJ*, 61, 321
 Obuljen A., Castorina E., Villaescusa-Navarro F., Viel M., 2018, *JCAP*, 5, 004
 Okamoto T., Frenk C. S., Jenkins A., Theuns T., 2010, *MNRAS*, 406, 208
 Olivari L. C., Dickinson C., Battye R. A., Ma Y.-Z., Costa A. A., Remazeilles M., Harper S., 2018, *MNRAS*, 473, 4242
 Oppenheimer B. D., Davé R., 2008, *MNRAS*, 387, 577
 Padmanabhan H., Refregier A., Amara A., 2017, *MNRAS*, 469, 2323
 Padmanabhan N. et al., 2007, *MNRAS*, 378, 852
 Pénin A., Umeh O., Santos M. G., 2018, *MNRAS*, 473, 4297
 Perlmutter S. et al., 1999, *ApJ*, 517, 565
 Raccanelli A. et al., 2015, *Advancing Astrophysics with the Square Kilometre Array (AASKA14)*, 31
 Ross A. J., Samushia L., Howlett C., Percival W. J., Burden A., Manera M., 2015, *MNRAS*, 449, 835
 Santos M. et al., 2015, *Advancing Astrophysics with the Square Kilometre Array (AASKA14)*, 19
 Sarkar D., Bharadwaj S., 2018, *MNRAS*, 476, 96
 Sarkar D., Bharadwaj S., Anathpindika S., 2016, *MNRAS*, 460, 4310
 Slosar A. et al., 2011, *Journal of Cosmology and Astro-Particle Physics*, 2011, 001
 Smith B. D. et al., 2016, *Grackle: Chemistry and radiative cooling library for astrophysical simulations. Astrophysics Source Code Library*
 Springel V., 2005, *MNRAS*, 364, 1105
 Springel V., 2010, *MNRAS*, 401, 791
 Springel V., Hernquist L., 2003, *MNRAS*, 339, 289
 Takahashi R., Sato M., Nishimichi T., Taruya A., Oguri M., 2012, *ApJ*, 761, 152
 Taruya A., Bernardeau F., Nishimichi T., Codis S., 2012, *Phys. Rev. D*, 86, 103528
 Taruya A., Nishimichi T., Saito S., 2010, *Phys. Rev. D*, 82, 063522
 Taruya A., Nishimichi T., Saito S., Hiramatsu T., 2009, *Phys. Rev. D*, 80, 123503
 Torrey P., Vogelsberger M., Genel S., Sijacki D., Springel V., Hernquist L., 2014, *MNRAS*, 438, 1985
 Umeh O., 2017, *JCAP*, 6, 005
 Viel M., Haehnelt M. G., Bolton J. S., Kim T.-S., Puchwein E., Nasir F., Wakker B. P., 2017, *MNRAS*, 467, L86
 Villaescusa-Navarro F., Alonso D., Viel M., 2017, *MNRAS*, 466, 2736
 Vogelsberger M., Genel S., Sijacki D., Torrey P., Springel V., Hernquist L., 2013, *MNRAS*, 436, 3031
 Vogelsberger M. et al., 2014, *MNRAS*, 444, 1518
 Wyithe J. S. B., Loeb A., Barnes D. G., 2005, *ApJ*, 634, 715
 Zhao G.-B. et al., 2016, *MNRAS*, 457, 2377